Article

Limited Domain SnSb@N-PC Composite Material as a High-Performance Anode for Sodium Ion Batteries

Zhaomeng Liu [1,2,*], Hailong Ren [1], Shizheng Fu [1], Wentao Yang [1], Yihua Li [1], Yang Jiao [1] and Botao Zhang [1]

[1] Institute for Energy Electrochemistry and Urban Mines Metallurgy, School of Metallurgy, Northeastern University, Wenhua Road, Heping District, Shenyang 110819, China; 2171660@stu.neu.edu.cn (H.R.); 20213485@stu.neu.edu.cn (S.F.); 20213323@stu.neu.edu.cn (W.Y.); 20213324@stu.neu.edu.cn (Y.L.); 20213536@stu.neu.edu.cn (Y.J.); 20213205@stu.neu.edu.cn (B.Z.)

[2] Key Laboratory of Advanced Energy Materials Chemistry (Ministry of Education), Nankai University, Tianjin 300071, China

* Correspondence: liuzhaomeng@smm.neu.edu.cn

Abstract: Anode materials have a vital influence on the performance of sodium ion batteries. In this paper, SnSb nanoparticles were distributed uniformly in N-doped three-dimensional porous carbon (SnSb@N-PC), which effectively avoided the agglomeration of alloy nanoparticles and greatly improved the capacity retention rate of SnSb@N-PC. At the same time, the porous carbon substrate brings higher conductivity, larger specific surface area, and more sodium storage sites, which makes the material obtain excellent sodium storage properties. The first discharge-specific capacity of SnSb@N-PC was 846.3 mAh g^{-1} at the current density of 0.1 A g^{-1}, and the specific capacity remained at 483 mAh g^{-1} after 100 cycles. Meanwhile, the specific capacity of SnSb@N-PC was kept at 323 mAh g^{-1} after 400 cycles at a high current density of 1.5 A g^{-1}, which indicated that the recombination of SnSb with porous carbon played a key role in the electrochemical performance of SnSb. The contribution of capacitance contrast capacity was able to reach more than 90% by the cyclic voltammetry (CV) test at high sweep speed, and larger Na^+ diffusivity was obtained by the constant current intermittent titration technique (GITT) test, which explains the good rate performance of SnSb@N-PC.

Keywords: sodium ion battery; anode; SnSb alloy; fast charge and store sodium; sodium storage mechanism

1. Introduction

With the rapid development of the economy, problems such as energy shortage and environmental pollution are becoming more and more serious, and it is urgent to develop clean and renewable energy [1–4]. It has become the consensus of the international community to promote green and low-carbon technology innovation and develop a modern energy system based on renewable energy [5–7]. Accelerating the transition to clean and low-carbon energy is a global trend [8–10]. The lithium-ion battery has emerged as the most practical energy storage solution due to its high energy density, extended cycle life, portability, and environmental friendliness. Therefore, it is widely used in electronic equipment, electric vehicles, and power grid energy storage fields [11–13]. However, due to the limited and uneven distribution of lithium resources, there is a contradiction between supply and demand, which causes concern about the cost of renewable energy and lithium-ion batteries. Therefore, it is urgent to develop new energy storage systems [14–17]. Sodium ion batteries (NIBs) are considered as one of the most promising electrochemical energy storage systems because of their abundant resources, high safety, and low price [18–20]. Improving the performance of anode materials, cathode anode materials, electrolytes, and other key components of NIBs has been widely studied, which is very important for designing high-performance NIBs to meet the needs of large-scale electrochemical energy storage [21–24].

Anode materials have a vital influence on the performance of sodium ion batteries [25–27]. Up to now, various anode materials, including insertion reactive (graphite anode, MXene, etc.), alloy reactive (Sn, Sb, P, etc.), and conversion (Co_3O_4, FeS_2, NiS/NiS_2, CoP, $CoS/CoSe$, CoSe, etc.), have been explored for NIBs [28–36]. Alloy materials have been widely concerned by researchers because of their high specific capacity of sodium storage, relatively high reaction potential, and high conductivity [37–39]. However, the poor reaction kinetics of alloy materials, huge volume changes, and irreversible structural deterioration in the process of sodium intercalation and desalination lead to pulverization of materials and rapid attenuation of specific capacity, which limit the application of alloy materials [40,41]. In order to solve these problems, a great deal of work including micro/nano-scale structure design, introduction of buffer matrix materials, preparation of multi-metallic compounds, and so on have been devoted to improving properties of alloy materials [42–44]. But up to now, the performance of alloy-based hosts is not satisfactory, which is very important for the design of high-performance NIBs [45]. Therefore, it is a key problem to explore high-performance anodes and promote the application of alloy materials in NIBs.

Among the various alloy anode materials, Sn and Sb as anodes for NIBs usually undergo serious structural degradation and large volume change ($Na_{15}Sn_4$ is about 424%, and Na_3Sb is about 390%) during sodiation/desodiation processes, which results in agglomeration, pulverization, and electrochemical inactivation [46–48]. Due to the different sodiation/desodiation of Sn and Sb, alloying can achieve the gradual formation of amorphous, nano-limited intermediate phases and the corresponding elastic softening of highly natrified Sn and Sb phases, which becomes an effective way to absorb and mitigate the large volume changes and material pulverization during Na^+ insertion/extraction [49–51]. Hence, SnSb alloys have received widespread attention as anode materials for NIBs. A series of unique SnSb alloys (such as SnSb microparticles, colloidal SnSb nanocrystals, and porous SnSb) and SnSb@C composites (such as SnSb@N-doped carbon, SnSb@porous carbon nanofibers, SnSb@carbon nanocable@graphene sheets, SnSb@graphene, SnSb@N-doped porous graphene network, and SnSb@N-rich porous carbon nanowires) have been lucubrated, which presents excellent Na^+ storage performances [46,49–55]. However, to meet the growing demand for high-power electric vehicles and large-scale energy storage systems and compete with LIBs and other emerging battery technologies, the rate performance and cycle stability of SnSb-based anode materials in NIBs need further improvement [56–58]. The corresponding Na^+ storage mechanism also needs to be further investigated [59–64]. At present, there are two significant issues should be addressed urgently for the development of SnSb-based anode materials in NIBs: how to obtain the fabrication of ultrasmall SnSb nanoparticles (e.g., <5 nm in diameter) and how to select the suitable substrates for SnSb alloys (currently mainly refer to carbon materials) [65–67].
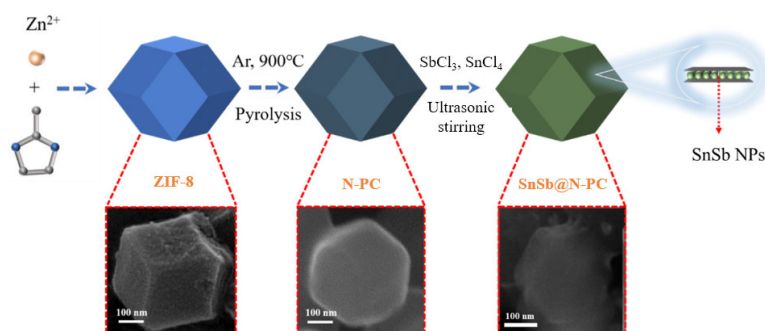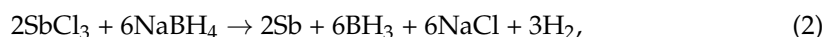
Recently, metal-organic frameworks (MOFs), especially the ZIF-8 system with the advantages of wide range of application, easy synthesis, and relatively excellent structural stability, have received a lot of attention as starting materials for carbon and carbon composites. An important application of MOFs is to combine with other materials to prepare ultra-small nanoparticle hybrids embedded in a carbon matrix [68]. For example, ultra-small Sn nanodots with a size of 2–3 nm were synthesized, and Sn particles have limited dispersion in N-doped mesoporous MOF-derived carbon substrates [69]. Yu et al. used the constraint effect of N-doped microporous carbon derived from ZIF-8 to prepare ultra-small red P nanoparticles with a diameter of <1 nm by the evaporation–condension–transformation method [70]. Jiao et al. reported that ultra-small Sn nanoparticles ($\approx$0.8 nm) were encapsulated in N-doped microporous carbon matrix derived from ZIF-8 by the chemical vapor transformation method [71]. However, the electrochemical properties of the materials obtained by the above experimental scheme are still lacking. In order to solve the above problems, it is very important to use the facial chemical reduction method based on liquid phase adsorption to reduce different metal ions to metal particles, which has the advantages of high efficiency, easy operation, and simple equipment, as well as

being conducive to the preparation of different kinds of nanoparticles [72]. However, the preparation of ultra-small SnSb nanoparticles by rapid reduction methods has not yet been reported, and this remains a challenge [73]. In addition, a suitable carbon substrate with small size and a large number of micropores plays an important role in the preparation of ultra-small alloy nanoparticles, avoiding the aggregation of alloy nanoparticles, and promoting the Na^+ insertion/extraction kinetics [74].

Herein, in order to solve the problem of excessive volume expansion of antimony during charge and discharge and the rapid decay of capacity caused by the material pulverization, we employed ZIF-8 as carbon substrate and successfully synthesized the N-doped three-dimensional porous carbon (N-PC)-supported SnSb@N-PC nanocomposites as anodes for rechargeable NIBs with the chemical reduction method and a subsequent thermal treatment process. N-doped three-dimensional porous carbon (N-PC) was selected as the matrix, which can store and limit the SnSb alloy particles. With $SbCl_3$ and $SnCl_4$ as raw materials, SnSb@N-PC composites with unique structure were prepared by the chemical reduction method with small size and limited domain. The special structure effectively avoided agglomeration of SnSb alloy nanoparticles. Therefore, the cycle stability of the material of SnSb@N-PC as an anode for NIBs was tested. SnSb@N-PC composites present a specific capacity of 483 mAh g^{-1} and maintained stable cycling after 100 cycles at 0.1 A g^{-1} current density, and it showed a high capacity of 323 mAh g^{-1} after 400 cycles at the current density of 1.5 A g^{-1}. Moreover, the porous carbon substrate brings higher conductivity, larger specific surface area, and more sodium storage sites. The diffusion coefficients of SnSb@N-PC composites are mainly about 10^{-11} cm^2 s^{-1}. As a result, the rate performance and sodium storage performance are significantly improved. On the basis of the ultrafast electrochemical performance, the SnSb@N-PC is a highly promising electrode material for sodium ion batteries and it may serve as an appropriate electrode material for other energy storage devices.

2. Results

Figure 1 shows the synthesis process of SnSb@N-PC composite. The size of ZIF-8 ranged from 150 nm to 200 nm. The sample was washed with 2.5 mol L^{-1} dilute HCl solution because Zn^{2+} was oxidized to Zn during high-temperature pyrolysis. In this process, the disappearance of Zn made a large number of micropores and mesopores appear in the samples (N-PC). Then, SnSb nanoparticles were uniformly distributed in the three-dimensional porous carbon materials using $SnCl_4$ and $SbCl_3$ as raw materials. Subsequently, the composites were characterized, and electrochemical tests were carried out. The corresponding reaction process of SnSb@N-PC is as follows:

$$Zn + 2HCl \rightarrow ZnCl_2 + H_2, \tag{1}$$

$$2SbCl_3 + 6NaBH_4 \rightarrow 2Sb + 6BH_3 + 6NaCl + 3H_2, \tag{2}$$

$$SnCl_4 + NaBH_4 \rightarrow Sn + BCl_3 + NaCl + 2H_2, \tag{3}$$

Figure 1. Schematic diagram of the synthesis process of SnSb@N-PC composites and the morphology of SnSb@N-PC.

3. Discussion

The XRD of SnSb@N-PC composite material is shown in Figure 2a. The positions of the characteristic peaks of SnSb@N-PC and pure bulk SnSb were basically the same. The diffraction peaks at 28.8°, 40.1°, 41.9°, 51.7°, 59.8°, 68.6°, and 75.8° corresponded to the (012), (104), (110), (202), (024), (122), and (009) crystal planes of Sb in SnSb and SnSb@N-PC by comparing with the SnSb standard card (JCPDS#33-0118), respectively. All the diffraction peaks were very sharp, and there were no obvious miscellaneous peaks, which shows that the alloy material had a high degree of crystallization, uniform composition, and ideal purity of the material. As shown in Figure 2b, Raman spectra of SnSb@N-PC were measured, where two typical peaks at 1342.58 and 1591.00 cm^{-1} belonged to the D band and G band of pyrolytic carbon, respectively. The D band can reflect the disorder and defect of carbon, while the G band can represent the in-plane stretching vibration of sp^2 hybrid carbon atoms. According to the strength of D-band and G-band, the intensity ratio of I_D/I_G is ≈ 1.02, it is obvious that there were a certain number of defects and disorders in N-PC, which is beneficial to improve the storage capacity of Na^+. The N_2 adsorption/desorption isotherms showed porous characteristics of SnSb@N-PC, which showed that the Brunauer–Emmett–Teller (BET) specific surface areas of the designed composite were 382.4 $m^2\,g^{-1}$. SnSb nanoparticles were coated by the N-PC carbon with limited self-agglomeration.
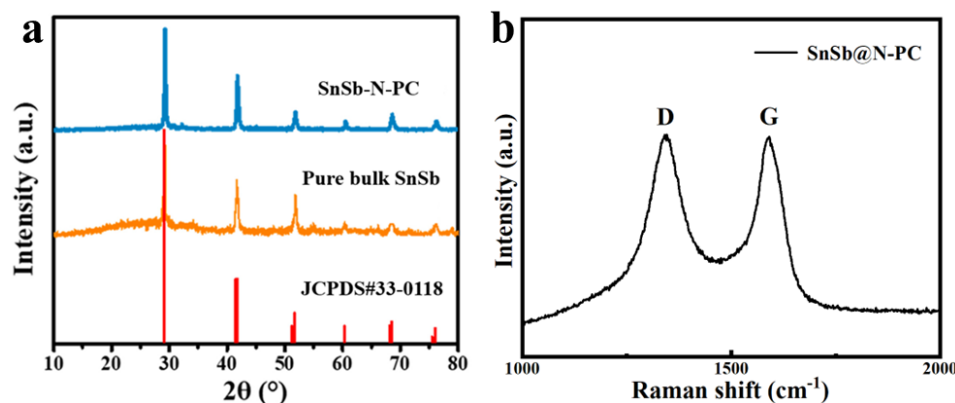

Figure 2. XRD (**a**) and Raman patterns (**b**) of SnSb@N-PC composite.

The morphology of SnSb@N-PC composites was characterized by SEM and TEM. According to the scanning electron microscope image of Figure 3a,b, it can be clearly found that the amorphous porous carbon was evenly dispersed on the dodecahedral nanosheets. The HRTEM diagram in Figure 3c presents the selected broken nanocomposite, in which several tens of nanometer-sized SnSb phases were homogeneously distributed throughout the particles. The typical characteristic interlayer shows the spacing of 0.299 nm and 0.200 nm, corresponding to the (1 0 1) lattice and (1 1 0) planes of the SnSb alloy, respectively. The lattice spacing of the short-range ordered pyrolytic carbon (0.34 nm) is not marked in Figure 3c because of the similar spacing of the (0 1 2) crystal face spacing in the SnSb alloy [50,53,56]. It was proven to be stable in MOF-derived carbon. The composite carbon structure can not only improve the conductivity of the material but can also accelerate the diffusion rate of ions, thus enhancing the electrochemical performance of the material [34,59]. Due to the large specific surface area of N-doped three-dimensional porous carbon, SnSb alloy particles can be prevented from accumulating by the limited domain of carbon, so that the grains do not agglomerate and exist in the form of nano-sized small particles. The element distribution diagram of the composite material (Figure 3d) shows that Sb, Sn, and N elements are uniformly distributed in the nanocomposite material, indicating that the MOF-derived nanocarbon material has been successfully doped with heteroatom (N element) during the sample preparation process [75], and the beneficial heteroatom doping is conducive to increasing the active site of the material, thereby improving the sodium storage performance of the material.
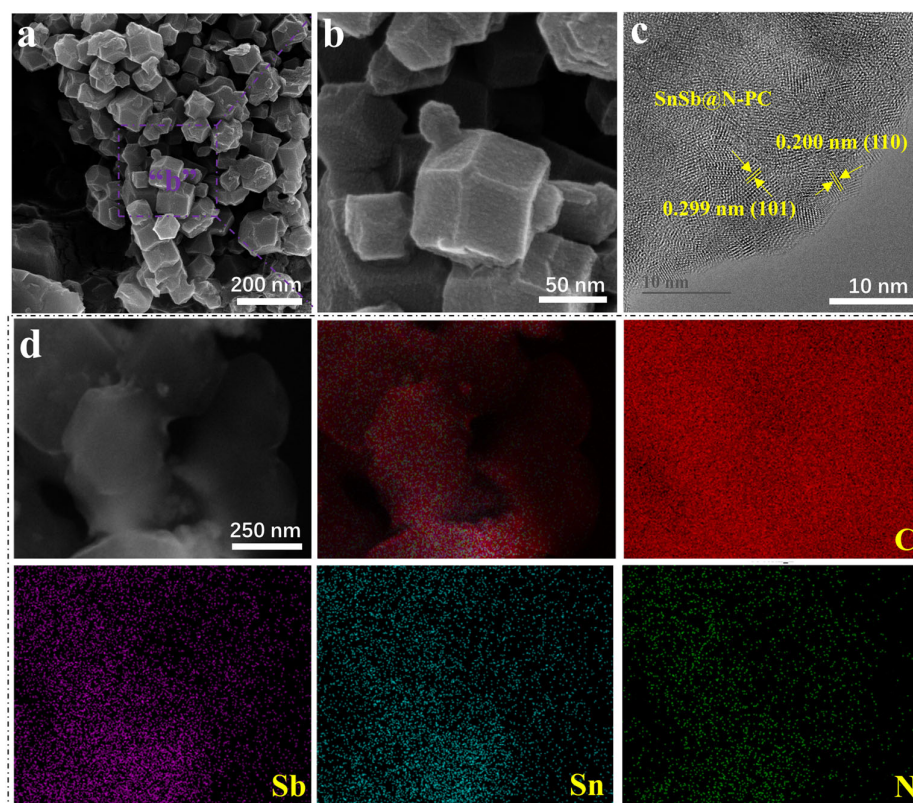
Figure 3. SEM (**a**,**b**); TEM (**c**); the corresponding EDS mappings; (**d**) images showing the elementary composition of C, Sb, Sn, N in the SnSb@N-PC composite.

In order to test the electrochemical performance of SnSb@N-PC nano-material as the negative electrode of sodium ion battery, it was assembled into a button half-cell for the CV test and constant current charge–discharge test. Figure 4a shows the CV curve of SnSb@N-PC composite electrode for three cycles in the first five cycles, with a scanning rate of 0.1 mV s^{-1} and a voltage range of 0.005–2.0 V (vs. Na$^+$/Na). It can be clearly seen that the CV curve of the first cycle was quite different from that of the other two cycles, which can mainly be attributed to the irreversible decomposition of electrolyte and the irreversible deintercalation of Na$^+$ in carbon and SnSb. For the first cathodic scan, the reduction peak at 1.0 V can be attributed to the formation of solid electrolyte interface (SEI) film on the alloy surface and the reduction of SnSb oxide. The reduction peak at 0.26 V can be attributed to the formation of Na$_{15}$Sn$_4$ and Na$_3$Sb by the alloying reaction of Na-Sn and Na-Sb. The reduction peak at about 0.01 V is related to Na$^+$ insertion into porous carbon. In anodic scanning, the first peak of 0.25 V can correspond to the removal of Na$^+$ from porous carbon. In addition, the reduction peak at about 1.0 V for the first cathodic scan disappeared in the subsequent scan, which can be attributed to the formation of SEI film. The alloying reaction occurred at about 0.72 V (Na$_x$Sb) and 0.49 V (Na$_3$Sb and Na$_{15}$Sn$_4$), starting with the second cathodic scan. In addition, the other scan curves coincided well after the first scan, which indicates that the electrode material has good reversibility of reaction. Figure 4b shows the constant current charge–discharge curves of the material at 0.1 A g^{-1} current density for the first, second, fifth, and tenth cycles. The plateau at about 0.5 V (vs. Na$^+$/Na) corresponded to the formation of SEI film in the first cycle discharge curve of SnSb@N-PC nanomaterials. The first discharge and charge capacity of SnSb@N-PC nanomaterials were 846.3 mAh g^{-1} and 451.8 mAh g^{-1}, respectively, and the first coulomb efficiency (CE) was only 53.4%. The lower initial coulomb efficiency can be attributed to the irreversible decomposition of electrolytes, the formation of SEI film, and the irreversible deintercalation of sodium ions in porous carbon. The specific capacity of the sample was stable at 516 mAh g^{-1}, and the coulomb efficiency reached 95.6% after ten cycles, which

shows the stability of electrode structure and cycle. Figure 4c–e shows the good cycle performance and rate ability of SnSb@N-PC nanomaterials. The first discharge specific capacity of SnSb@N-PC was 846.3 mAh g^{-1} at 0.1 A g^{-1} current density, and the specific capacity remained at 483 mAh g^{-1} after 100 cycles. At the same time, the specific capacity was kept at 323 mAh g^{-1} after 400 cycles at a high current density of 1.5 A g^{-1}.
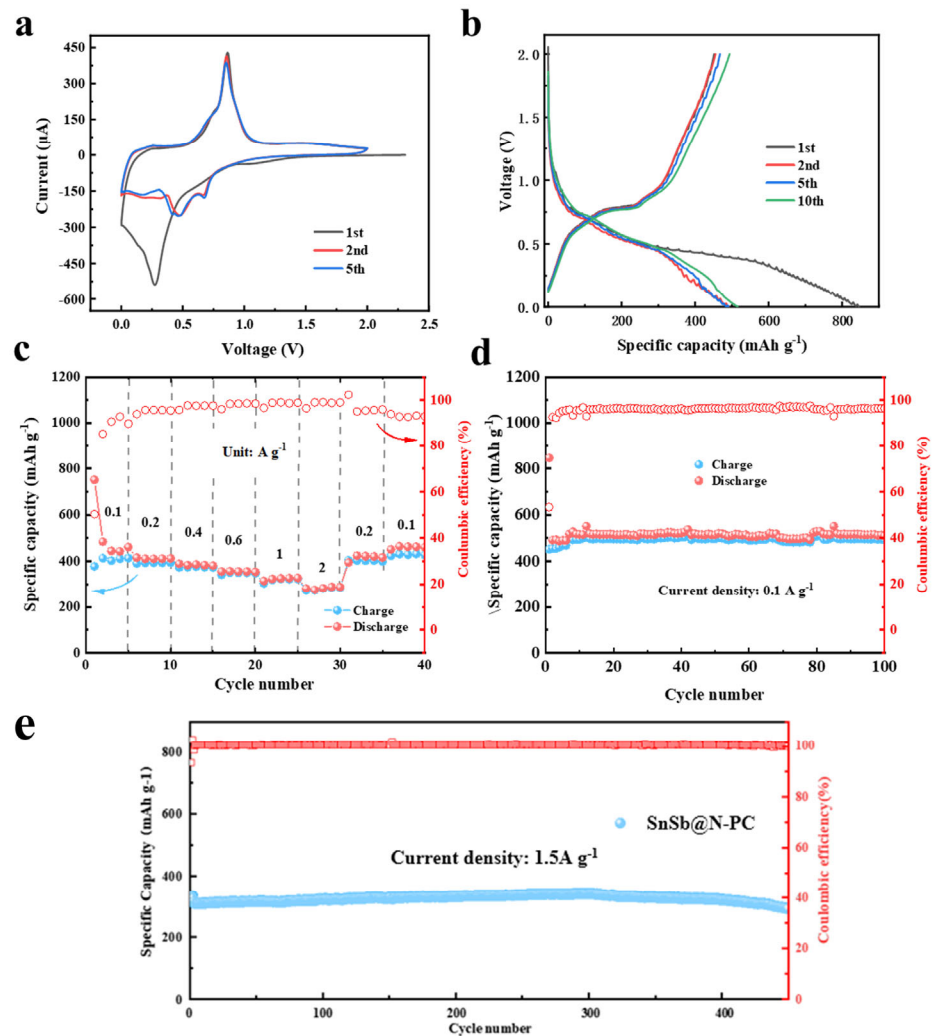
Figure 4. Electrochemical performance of SnSb@N-PC nanomaterials as anodes for sodium ion batteries (**a**) CV curves for the first, second, and fifth turns. (**b**) Charge/discharge curves for the first, second, fifth, and tenth turns. (**c**) Multiplicity performance at 0.1 A g^{-1}–2 A g^{-1}. (**d**) Cycling performance of SnSb@N-PC at 0.1 A g^{-1}. (**e**) Cycling performance of SnSb@N-PC at 1.5 A g^{-1}.

In order to further analyze the kinetics of sodium storage in SnSb@N-PC anode materials, the CV curves of sodium ion batteries were measured at different sweep rates (0.1, 0.2, 0.5, 1.0, 2.0 mV s^{-1}). Figure 5a shows that the shape of the curve did not change obviously with the increase in scanning speed, so SnSb@N-PC had good stability. However, the area of the CV curve increased with the increase in scanning speed, which indicates that there was a capacitive sodium storage behavior on the electrode surface. The behavior of peak current is analyzed by Equation (3) in this paper [76,77].

$$i = a\, v^{b} \tag{4}$$

where a is a constant and v is the scanning speed. The b value is the slope of the ln i and ln v graphs where the b value can vary between 0.5 and 1.0, which shows that the specific capacity of the electrode is dominated by diffusion process and capacitance drive,

respectively. The b value of the negative electrode gradually increased from 0.55 to 0.97 with the increase in scanning speed, which indicated that the electrochemical reaction of SnSb@N-PC negative electrode was controlled by the combination of capacitance and diffusion process (Figure 5b). In addition, according to the Equation (4), the specific proportion of the contribution of capacitance ($k_1 v$) and diffusion-controlled effects ($k_2 v^{1/2}$) to the material capacity is discussed.

$$i\,(V) = k_1\,v + k_2\,v^{1/2} \tag{5}$$
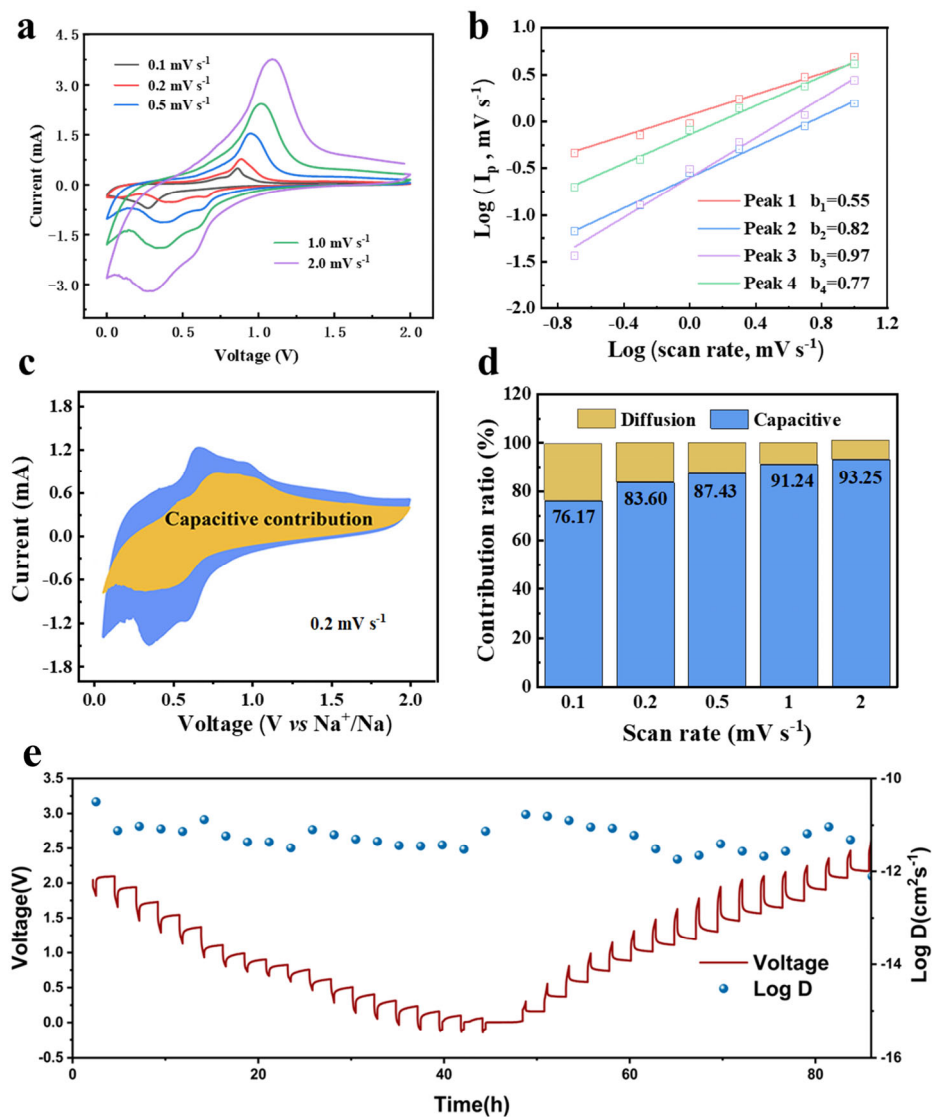
Figure 5. (**a**) CV curves of SnSb@N-PC at different sweep rates. (**b**) Scan index b values calculated according to Figure 4a. (**c**) Capacitive contribution capacity ratio of SnSb@N-PC at a scan rate of 0.2 mV s^{-1}. (**d**) Capacitive and diffusion contribution capacity ratio of SnSb@N-PC for different sweep rates. (**e**) The GITT curve and the diffusion rate calculated from the GITT curve of SnSb@N-PC.

As shown in Figure 5c, the capacitive capacity contribution accounted for 83.6% in the CV curve with a scanning speed of 0.2 mV s^{-1}. The capacitance contributions were 76.17%, 83.60%, 87.43%, 91.24%, and 93.25% at the scanning rates of 0.1, 0.2, 0.5, 1, and 2 mV s^{-1}, respectively (Figure 5d). The capacitance effect dominated the storage behavior of Na$^+$ under high current, which is beneficial to the structural stability of materials, and this is also the main reason for the excellent cycle and rate performance. Figure 5e further shows the sodium ion diffusion coefficient of the SnSb@N-PC anode calculated according

to the GITT curve, which can analyze the diffusion behavior of Na$^+$ in solid-phase electrode charging and discharging. The measured diffusion coefficients of Na$^+$ in active materials ranged from 10^{-12} to 10^{-10} cm^2 s^{-1} and was mainly concentrated in about 10^{-11} cm^2 s^{-1}. Combining the above results, the three-dimensional porous carbon had a positive effect on the electrochemical behavior of the SnSb@N-PC electrode by improving the sodium ion diffusion coefficient during the cycling process. This structure makes the electrolyte fully infiltrated, has high conductivity, promotes ion migration, and prevents alloy particles from agglomerating.

4. Materials and Methods

4.1. Preparation of SnSb@N-PC

Firstly, a ZIF-8 metal-organic framework synthesized by coordination chelation of dimethylimidazole ($C_4H_6N_2$) and Zn^{2+} was used as a precursor [78]. The ZIF-8 nanocrystals were heated to 300 °C for 2 h and then carbonized at 900 °C for 5 h at a heating rate of 5 °C/min. Subsequently, the sample was washed with 2.5 mol L^{-1} dilute HCl solution. Finally, the sample was washed repeatedly with deionized water and dried in vacuum at 70 °C for 12 h. Porous structure with N doping (N-PC) with a large number of micropores and mesopores was obtained, and high homogeneity of in situ N doping was achieved. Then, 40 mg of the prepared N-PC powder was diluted in a 40 mL solution of SnCl$_4$ (140 mg) and SbCl$_3$ (91.2 mg) in methanol and stirred at room temperature for 3 h. Subsequently, a 2 mL solution of methanol NaBH$_4$ (200 mg) was then rapidly added to the mixture, which was then magnetically stirred at room temperature for 30 min. The mixture was centrifuged, washed with deionized water and methanol, and dried in a vacuum drying oven at 70 °C for 12 h. The above steps are repeated without adding porous carbon to obtain SnSb@N-PC.

4.2. Characterization

In order to study the morphology, crystal structure, and chemical composition of the samples, X-ray diffraction (XRD) was used to characterize the samples. The X-ray diffraction instrument (D 8, Cu K α irradiation, λ = 0.154 nm, 40 kV, 2 θ = 20~80°) is manufactured by Bruker. A scanning electron microscope (SEM, Zeiss, Oberkochen, Germany, 15 kV) and transmission electron microscope (TEM, FEI, 200 Kv, Portland, OR, USA) were also used to analyze the samples. The corresponding EDS Mappings was tested using One Max 20 equipment. Raman spectroscopy (Senterra, Bruker, Karlsruhe, Germany) was also used to characterize the disorder and defects of carbon materials.

4.3. Electrochemical Measurements

Firstly, the active material, acetylene carbon black and polyvinylidene fluoride (PVDF) were weighed and mixed evenly according to the mass ratio of 8:1:1. N-methyl pyrrolidone (NMP) was used as solvent to form a uniform slurry, which was coated on copper foil. The electrodes were then dried in a vacuum oven at 80 °C for 12 h. The button half-cell was fabricated with sodium as counter electrode, glass superfine fiber as the separator and 1 M NaPF$_6$ in EC/DEC as the electrolyte. The LAND battery instrument (Wuhan Kingnuo Electronic Co., Wuhan, China) was used to conduct the constant current charge and discharge test and galvanostatic intermittent titration technique (GITT) test. The cyclic voltammetry test (CV, scanning speed 0.1–1 mV s^{-1}) was measured in an electrochemical workstation (CHI660E) with a voltage window of 0.005–2 V. The apparent diffusion coefficients of Na$^+$ in the electrode were measured by GITT [37]. The ratio of capacitance drive and diffusion process to total capacity was calculated [79].

Equation (3) is the apparent diffusion coefficients of Na$^+$.

$$D_k = \frac{4}{\pi\tau}\left(\frac{m_B V_m}{M_B S}\right)\left(\frac{\Delta E_S}{\Delta E_\tau}\right)^2 \left(\ll \frac{I^2}{D_k}\right) \tag{6}$$

where m_B and M_B are the mass of the active substance and molecular weight, respectively; S is the total contact area between the electrolyte and the electrode; V_m is the molar volume of the active substance; I is the thickness of the electrode; and ΔE_s and ΔE_τ are the steady-state voltage change after subtracting the voltage drop and the total transient change in cell voltage during a single titration, respectively.

5. Conclusions

SnSb@N-PC composite was successfully prepared with $SbCl_3$, $SnCl_4$, and N-PC as raw materials, in which SnSb nanoparticles were uniformly distributed in three-dimensional porous carbon materials. The special composite structure greatly avoided the agglomeration of alloy nanoparticles during synthesis process, which improved the capacity retention of SnSb@N-PC composite. On the other hand, the high conductivity, larger specific surface area, and more sodium storage sites brought by porous carbon substrate materials make SnSb@N-PC composites obtain excellent sodium storage performance. The specific capacity of SnSb@N-PC composites was maintained at 483 mAh g^{-1} after 100 cycles at 0.1 A g^{-1} current density, and at 323 mAh g^{-1} after 400 cycles at 1.5 A g^{-1} current density. The results of the CV test show that the sodium storage process of SnSb@N-PC composites is controlled by the combination of capacitive and diffusion processes, and the contribution of capacitance to capacity can reach more than 90% at high scanning speed. The diffusion coefficients of SnSb@N-PC composites were mainly about 10^{-11} cm^2 s^{-1}. Therefore, SnSb@N-PC composites have good rate performance.

Author Contributions: Conceptualization, Z.L. and H.R.; methodology, Z.L.; software, H.R.; validation, Z.L., S.F. and W.Y.; formal analysis, Y.L.; resources, Z.L.; data curation, H.R. and Z.L.; writing—original draft preparation, Z.L. and Y.J.; investigation, Z.L. and B.Z.; writing—review and editing, Z.L.; visualization, S.F.; supervision, Z.L.; project administration, Z.L.; funding acquisition, Z.L. All authors have read and agreed to the published version of the manuscript.

Data Availability Statement: The original contributions presented in the study are included in the article, further inquiries can be directed to the corresponding authors.

Conflicts of Interest: The authors declare no conflicts of interest.

References

1. Ge, J.; Fan, L.; Wang, J.; Zhang, Q.; Liu, Z.; Zhang, E.; Liu, Q.; Yu, X.; Lu, B. MoSe$_2$/N-Doped Carbon as Anodes for Potassium-Ion Batteries. *Adv. Energy Mater.* **2018**, *8*, 1801477. [CrossRef]
2. Mu, J.; Zhao, Z.; Gao, X.W.; Liu, Z.M.; Luo, W.B.; Sun, Z.; Gu, Q.F.; Li, F. Bimetallic PdFe$_3$ Nano-Alloy with Tunable Electron Configuration for Boosting Electrochemical Nitrogen Fixation. *Adv. Energy Mater.* **2023**, *14*, 2303558. [CrossRef]
3. Zhao, L.K.; Gao, X.W.; Mu, J.; Luo, W.B.; Liu, Z.; Sun, Z.; Gu, Q.F.; Li, F. Durable Integrated K-Metal Anode with Enhanced Mass Transport through Potassiphilic Porous Interconnected Mediator. *Adv. Funct. Mater.* **2023**, *33*, 2304292. [CrossRef]
4. Yu, W.; Ge, J.; Hu, Y.; Shen, D.; Luo, W.; Chen, S.; Wu, L.; Liu, Z.; Zhou, J.; Yang, H.; et al. Hybrid High-Performance Aqueous Batteries with Potassium-Based Cathode||Zinc Metal Anode. *Sci. China Mater.* **2022**, *66*, 923–931. [CrossRef]
5. Liu, Z.; Wang, J.; Ding, H.; Chen, S.; Yu, X.; Lu, B. Carbon Nanoscrolls for Aluminum Battery. *ACS Nano* **2018**, *12*, 8456–8466. [CrossRef]
6. Liu, Z.; Wang, J.; Jia, X.; Li, W.; Zhang, Q.; Fan, L.; Ding, H.; Yang, H.; Yu, X.; Li, X.; et al. Graphene Armored with a Crystal Carbon Shell for Ultrahigh-Performance Potassium Ion Batteries and Aluminum Batteries. *ACS Nano* **2019**, *13*, 10631–10642. [CrossRef]
7. Wang, J.; Fan, L.; Liu, Z.; Chen, S.; Zhang, Q.; Wang, L.; Yang, H.; Yu, X.; Lu, B. In Situ Alloying Strategy for Exceptional Potassium Ion Batteries. *ACS Nano* **2019**, *13*, 3703–3713. [CrossRef]
8. Zhu, Z.; Jiang, T.; Ali, M.; Meng, Y.; Jin, Y.; Cui, Y.; Chen, W. Rechargeable Batteries for Grid Scale Energy Storage. *Chem. Rev.* **2022**, *122*, 16610–16751. [CrossRef]
9. Wang, F.; Wu, X.; Li, C.; Zhu, Y.; Fu, L.; Wu, Y.; Liu, X. Nanostructured positive electrode materials for post-lithium ion batteries. *Energy Environ. Sci.* **2016**, *9*, 3570–3611. [CrossRef]

10. Wang, W.; Yuan, B.; Sun, Q.; Wennersten, R. Application of energy storage in integrated energy systems—A solution to fluctuation and uncertainty of renewable energy. *J. Energy Storage* **2022**, *52*, 104812. [CrossRef]

11. Li, J.; Fleetwood, J.; Hawley, W.B.; Kays, W. From Materials to Cell: State-of-the-Art and Prospective Technologies for Lithium-Ion Battery Electrode Processing. *Chem. Rev.* **2022**, *122*, 903–956. [CrossRef]

12. Yuan, S.; Lai, Q.; Duan, X.; Wang, Q. Carbon-based materials as anode materials for lithium-ion batteries and lithium-ion capacitors: A review. *J. Energy Storage* **2023**, *61*, 106716. [CrossRef]

13. Xiang, J.; Wei, Y.; Zhong, Y.; Yang, Y.; Cheng, H.; Yuan, L.; Xu, H.; Huang, Y. Building Practical High-Voltage Cathode Materials for Lithium-Ion Batteries. *Adv. Mater.* **2022**, *34*, 2200912. [CrossRef]

14. Mohr, S.H.; Mudd, G.M.; Giurco, D. Lithium Resources and Production: Critical Assessment and Global Projections. *Minerals* **2012**, *2*, 65–84. [CrossRef]

15. Grosjean, C.; Miranda, P.H.; Perrin, M.; Poggi, P. Assessment of world lithium resources and consequences of their geographic distribution on the expected development of the electric vehicle industry. *Renew. Sustain. Energy Rev.* **2012**, *16*, 1735–1744. [CrossRef]

16. Wanger, T.C. The Lithium future—Resources, recycling, and the environment. *Conserv. Lett.* **2011**, *4*, 202–206. [CrossRef]

17. Pavlovskii, A.A.; Pushnitsa, K.; Kosenko, A.; Novikov, P.; Popovich, A.A. A Minireview on the Regeneration of NCM Cathode Material Directly from Spent Lithium-Ion Batteries with Different Cathode Chemistries. *Inorganics* **2022**, *10*, 141. [CrossRef]

18. Nayak, P.K.; Yang, L.; Brehm, W.; Adelhelm, P. From Lithium-Ion to Sodium-Ion Batteries: Advantages, Challenges, and Surprises. *Angew. Chem. Int. Ed.* **2018**, *57*, 102–120. [CrossRef]

19. Gu, X.; Gao, X.-W.; Yang, D.; Gu, Q.; Song, Y.; Chen, H.; Ren, T.; Luo, W.-B. Two positive effects with one arrow: Modulating crystal and interfacial decoration towards high-potential cathode material. *J. Energy Chem.* **2024**, *92*, 216–223. [CrossRef]

20. Mu, J.-J.; Liu, Z.-M.; Lai, Q.-S.; Wang, D.; Gao, X.-W.; Yang, D.-R.; Chen, H.; Luo, W.-B. An industrial pathway to emerging presodiation strategies for increasing the reversible ions in sodium-ion batteries and capacitors. *Energy Mater.* **2022**, *2*, 200043. [CrossRef]

21. Yang, S.; Wang, B.; Lv, Q.; Zhang, N.; Zhang, Z.; Jing, Y.; Li, J.; Chen, R.; Wu, B.; Xu, P.; et al. Recent Advances in Cathodes for All-Solid-State Lithium-Sulfur Batteries. *Chin. Chem. Lett.* **2023**, *34*, 107783. [CrossRef]

22. Ye, H.; Lei, D.; Shen, L.; Ni, B.; Li, B.; Kang, F.; He, Y.-B. In-Situ Polymerized Cross-Linked Binder for Cathode in Lithium-Sulfur Batteries. *Chin. Chem. Lett.* **2020**, *31*, 570–574. [CrossRef]

23. Zhang, R.; Wu, Z.; Huang, Z.; Guo, Y.; Zhang, S.; Zhao, Y.; Zhi, C. Recent Advances for Zn-Gas Batteries Beyond Zn-Air/Oxygen Battery. *Chin. Chem. Lett.* **2023**, *34*, 107600. [CrossRef]

24. Wang, Q.; Li, J.; Jin, H.; Xin, S.; Gao, H. Prussian-Blue Materials: Revealing New Opportunities for Rechargeable Batteries. *InfoMat* **2022**, *4*, e12311. [CrossRef]

25. Cao, L.; Gao, X.; Zhang, B.; Ou, X.; Zhang, J.; Luo, W.-B. Bimetallic Sulfide Sb_2S_3@FeS_2 Hollow Nanorods as High-Performance Anode Materials for Sodium-Ion Batteries. *ACS Nano* **2020**, *14*, 3610–3620. [CrossRef]

26. Bai, X.; Wu, N.; Yu, G.; Li, T. Recent Advances in Anode Materials for Sodium-Ion Batteries. *Inorganics* **2023**, *11*, 289. [CrossRef]

27. Fedoseeva, Y.V.; Shlyakhova, E.V.; Stolyarova, S.G.; Vorfolomeeva, A.A.; Nishchakova, A.D.; Grebenkina, M.A.; Makarova, A.A.; Kovalenko, K.A.; Okotrub, A.V.; Bulusheva, L.G. Electrochemical Performance of Potassium Hydroxide and Ammonia Activated Porous Nitrogen-Doped Carbon in Sodium-Ion Batteries and Supercapacitors. *Inorganics* **2022**, *10*, 198. [CrossRef]

28. Liu, Q.; Xu, R.; Mu, D.; Tan, G.; Gao, H.; Li, N.; Chen, R.; Wu, F. Progress in Electrolyte and Interface of Hard Carbon and Graphite Anode for Sodium-Ion Battery. *Carbon Energy* **2022**, *4*, 458–479. [CrossRef]

29. Wang, Q.; Ding, X.; Li, J.; Jin, H.; Gao, H. Minimizing the Interfacial Resistance for a Solid-State Lithium Battery Running at Room Temperature. *Chem. Eng. J.* **2022**, *488*, 137740. [CrossRef]

30. Liu, W.; Liu, W.; Jiang, Y.; Gui, Q.; Ba, D.; Li, Y.; Liu, J. Binder-Free Electrodes for Advanced Potassium-Ion Batteries: A Review. *Chin. Chem. Lett.* **2021**, *32*, 1299–1308. [CrossRef]

31. Yang, M.; Sun, Z.; Nie, P.; Yu, H.; Zhao, C.; Yu, M.; Luo, Z.; Geng, H.; Wu, X. $SbPS_4$: A Novel Anode for High-Performance Sodium-Ion Batteries. *Chin. Chem. Lett.* **2022**, *33*, 470–474. [CrossRef]

32. Mu, J.; Gao, X.-W.; Liu, Z.; Luo, W.-B.; Sun, Z.; Gu, Q.; Li, F. Boosting Nitrogen Electrocatalytic Fixation by Three-Dimensional $TiO_{2-\&}N_{\&}$ Nanowire Arrays. *J. Energy Chem.* **2022**, *75*, 293–300.

33. Wang, D.; Liu, Z.; Gao, X.-W.; Gu, Q.; Zhao, L.; Luo, W.-B. Massive Anionic Fluorine Substitution Two-Dimensional δ-MnO_2 Nanosheets for High-Performance Aqueous Zinc-Ion Battery. *J. Energy Storage* **2023**, *72*, 108740. [CrossRef]

34. Li, J.-G.; Mu, J.-J.; Liu, Z.-M.; Lai, Q.-S.; Zhao, L.-K.; Gao, X.-W.; Yang, D.-R.; Chen, H.; Luo, W.-B. Boosting Potassium-Based Dual Ion Battery With High Energy Density and Long Lifespan by Red Phosphorous. *J. Power Sources* **2023**, *571*, 233054. [CrossRef]

35. Liu, Z.; Peng, W.; Shih, K.; Wang, J.; Wang, Z.; Guo, H.; Yan, G.; Li, X.; Song, L. A MoS_2 Coating Strategy to Improve the Comprehensive Electrochemical Performance of $LiVPO_4F$. *J. Power Sources* **2016**, *315*, 294–301. [CrossRef]

36. Wang, J.; Liu, Z.; Yan, G.; Li, H.; Peng, W.; Li, X.; Song, L.; Shih, K. Improving the Electrochemical Performance of Lithium Vanadium Fluorophosphate Cathode Material: Focus on Interfacial Stability. *J. Power Sources* **2016**, *329*, 553–557. [CrossRef]

37. Wang, S.-S.; Liu, Z.-M.; Gao, X.-W.; Wang, X.-C.; Chen, H.; Luo, W.-B. Layer-Structured Multitransition-Metal Oxide Cathode Materials for Potassium-Ion Batteries with Long Cycling Lifespan and Superior Rate Capability. *ACS Appl. Mater. Interfaces* **2023**, *15*, 57165–57173. [CrossRef]

38. Wang, J.; Liu, Z.; Zhou, J.; Han, K.; Lu, B. Insights into Metal/Metalloid-Based Alloying Anodes for Potassium Ion Batteries. *ACS Mater. Lett.* **2021**, *3*, 1572–1598. [CrossRef]

39. Cheng, N.; Fan, L.; Liu, Z.; Chen, S.; Zhang, E.; Zhao, J.; Yang, H.; Yu, X.; Lu, B. Fluorine Atom-Inducing Graphene Oxide in situ Coating SnPO Composites as Anode for Sodium Ion Batteries. *Mater. Today Energy* **2019**, *11*, 174–181. [CrossRef]

40. Zhang, W.; Mao, J.; Li, S.; Chen, Z.; Guo, Z. Phosphorus-Based Alloy Materials for Advanced Potassium-Ion Battery Anode. *J. Am. Chem. Soc.* **2017**, *139*, 3316–3319. [CrossRef]

41. Balogun, M.-S.; Luo, Y.; Qiu, W.; Liu, P.; Tong, Y. A review of carbon materials and their composites with alloy metals for sodium ion battery anodes. *Carbon* **2016**, *98*, 162–178. [CrossRef]

42. Borah, R.; Hughson, F.R.; Johnston, J.; Nann, T. On battery materials and methods. *Mater. Today Adv.* **2020**, *6*, 100046. [CrossRef]

43. Palomares, V.; Casas-Cabanas, M.; Castillo-Martínez, E.; Han, M.H.; Rojo, T. Update on Na-based battery materials. A growing research path. *Energy Environ. Sci* **2013**, *6*, 2312–2337. [CrossRef]

44. Wang, L.; Tian, H.; Yao, X.; Cai, Y.; Gao, Z.; Su, Z. Research Progress and Modification Measures of Anode and Cathode Materials for Sodium-Ion Batteries. *ChemElectroChem* **2024**, *11*, e202300414. [CrossRef]

45. Shi, H.; Gao, X.-W.; Wang, X.; Chen, H.; Han, W.; Gu, Q.; Liu, Z.; Luo, W.-B. Surface Residual Alkali Reverse Utilization: Stabilizing the Lay-Structured Oxide Cathode for High Stability Potassium Ion Batteries. *Chem. Eng. J.* **2024**, *484*, 149574. [CrossRef]

46. Xie, H.; Tan, X.; Luber, E.J.; Olsen, B.C.; Kalisvaart, W.P.; Jungjohann, K.L.; Mitlin, D.; Buriak, J.M. β-SnSb for Sodium Ion Battery Anodes: Phase Transformations Responsible for Enhanced Cycling Stability Revealed by In Situ TEM. *ACS Energy Lett.* **2018**, *3*, 1670–1676. [CrossRef]

47. Zhang, D.M.; Jia, J.H.; Yang, C.C.; Jiang, Q. Fe_7Se_8 Nanoparticles Anchored on N-doped Carbon Nanofibers as High-Rate Anode for Sodium-Ion Batteries. *Energy Storage Mater.* **2020**, *24*, 439–449. [CrossRef]

48. Wang, Y.; Wen, Z.; Wang, C.C.; Yang, C.C.; Jiang, Q. MOF-Derived Fe_7S_8 Nanoparticles/N-Doped Carbon Nanofibers as an Ultra-Stable Anode for Sodium-Ion Batteries. *Small* **2021**, *17*, 2102349. [CrossRef]

49. Choi, J.-H.; Ha, C.-W.; Choi, H.-Y.; Lee, S.-M. Carbon Embedded SnSb Composite Tailored by Carbothermal Reduction Process as High Performance Anode for Sodium-Ion Batteries. *J. Ind. Eng. Chem.* **2018**, *60*, 451–457. [CrossRef]

50. Choi, J.-H.; Ha, C.-W.; Choi, H.-Y.; Seong, J.-W.; Park, C.-M.; Lee, S.-M. Porous Carbon-Free SnSb Anodes for High-Performance Na-Ion Batteries. *J. Power Sources* **2018**, *386*, 34–39. [CrossRef]

51. He, M.; Walter, M.; Kravchyk, K.V.; Erni, R.; Widmer, R.; Kovalenko, M.V. Monodisperse SnSb Nanocrystals for Li-ion and Na-ion Battery Anodes: Synergy and Dissonance Between Sn and Sb. *Nanoscale* **2015**, *7*, 455–459. [CrossRef]

52. Jia, H.; Dirican, M.; Chen, C.; Zhu, J.; Zhu, P.; Yan, C.; Li, Y.; Dong, X.; Guo, J.; Zhang, X. Reduced Graphene Oxide-Incorporated SnSb@CNF Composites as Anodes for High-Performance Sodium-Ion Batteries. *ACS Appl. Mater. Interfaces* **2018**, *10*, 9696–9703. [CrossRef]

53. Cheng, D.; Wei, A.; Ye, L.; Xu, G.; Tan, L.; Lu, B.; Chen, Y. Interfacial Bonding of SnSb Alloys with Graphene toward Ultrafast and Cycle-Stable Na-Ion Battery Anodes. *ACS Sustain. Chem. Eng.* **2022**, *10*, 12177–12187. [CrossRef]

54. Ji, L.; Gu, M.; Shao, Y.; Li, X.; Engelhard, M.H.; Arey, B.W.; Wang, W.; Nie, Z.; Xiao, J.; Wang, C.; et al. Controlling SEI Formation on SnSb-Porous Carbon Nanofi bers for Improved Na Ion Storage. *Adv. Mater.* **2014**, *26*, 2901–2908. [CrossRef]

55. Yue, L.; Jayapal, M.; Cheng, X.; Zhang, T.; Chen, J.; Ma, X.; Dai, X.; Lu, H.; Guan, R.; Zhang, W. Highly Dispersed Ultra-Small Nano Sn-SnSb Nanoparticles Anchored on Ndoped Graphene Sheets as High Performance Anode for Sodium Ion Batteries. *Appl. Surf. Sci.* **2020**, *512*, 145686. [CrossRef]

56. Li, C.; Pei, Y.R.; Zhao, M.; Yang, C.C.; Jiang, Q. Sodium Storage Performance of Ultrasmall SnSb Nanoparticles. *Chem. Eng. J.* **2021**, *40*, 129617. [CrossRef]

57. Darwiche, A.; Sougrati, M.T.; Fraisse, B.; Stievano, L.; Monconduit, L. Facile Synthesis and Long Cycle Life of SnSb as Negative Electrode Material for Na-Ion Batteries. *Electrochem. Commun.* **2013**, *32*, 18–21. [CrossRef]

58. Lu, Y.C.; Dimov, N.; Okada, S.; Bui, T.H. SnSb Alloy Blended with Hard Carbon as Anode for Na-Ion Batteries. *Energies* **2018**, *11*, 1614. [CrossRef]

59. Bian, Y.H.; Gao, X.W.; Zhao, L.K.; Liu, Z.; Gu, Q.; Luo, W.B. Enhanced Polysulfides Adsorption and Conversion for High Coulombic Efficiency Sodium-Ion Batteries. *Batter. Supercaps* **2023**, *6*, e202300227. [CrossRef]

60. Lai, Q.S.; Mu, J.J.; Liu, Z.M.; Zhao, L.K.; Gao, X.W.; Yang, D.R.; Chen, H.; Luo, W.B. Tunnel-Type $Na_2Ti_6O_{13}$@Carbon Nanowires as Anode Materials for Low-Temperature Sodium-Ion Batteries. *Batter. Supercaps* **2023**, *6*, e202200549. [CrossRef]

61. Yang, D.; Gao, X.W.; Gao, G.; Lai, Q.; Ren, T.; Gu, Q.; Liu, Z.; Luo, W.B. Local Electronic Structure Constructing of Layer-Structured Oxide Cathode Material for High-Voltage Sodium-Ion Batteries. *Carbon Energy* **2024**, e574. [CrossRef]

62. Zhao, L.-K.; Gao, X.-W.; Gu, Q.; Ge, X.; Ding, Z.; Liu, Z.; Luo, W.-B. Realizing a Dendrite-Free Metallic-Potassium Anode using Reactive Prewetting Chemistry. *eScience* **2023**, *4*, 100201. [CrossRef]

63. Zhao, L.-K.; Gao, X.-W.; Ren, T.-Z.; Wang, D.; Wang, D.-W.; Liu, Z.-M.; Chen, H.; Luo, W.-B. Regulating Ion Transport Behaviors toward Dendrite-Free Potassium Metal Batteries: Recent Advances and Perspectives. *Rare Met.* **2024**, *43*, 1435–1460. [CrossRef]

64. Liu, Z.; Wang, J.; Lu, B. Plum Pudding Model Inspired $KVPO_4F$@3DC as High-Voltage and Hyperstable Cathode for Potassium Ion Batteries. *Sci. Bull.* **2020**, *65*, 1242–1251. [CrossRef]

65. Wang, J.; Wang, B.; Liu, Z.; Fan, L.; Zhang, Q.; Ding, H.; Wang, L.; Yang, H.; Yu, X.; Lu, B. Nature of Bimetallic Oxide Sb_2MoO_6/rGO Anode for High-Performance Potassium-Ion Batteries. *Adv. Sci.* **2019**, *6*, 1900904. [CrossRef]

66. Cheng, N.; Zhao, J.; Fan, L.; Liu, Z.; Chen, S.; Ding, H.; Yu, X.; Liu, Z.; Lu, B. Sb-MOFs Derived Sb Nanoparticles@Porous Carbon for High Performance Potassium-Ion Batteries Anode. *Chem. Commun.* **2019**, *55*, 12511–12514. [CrossRef]

67. Ding, H.; Wang, J.; Fan, L.; Liu, Z.; Jia, X.; Yu, X.; Lu, B. Sn-Sb compounds with novel structure for stable potassium storage. *Chem. Eng. J.* **2020**, *395*, 125147. [CrossRef]

68. Jia, M.; Jin, Y.; Zhao, C.; Zhao, P.; Jia, M. High Electrochemical Sodium Storage Performance of ZnSe/CoSe@N-Doped Porous Carbon Synthesized by the in-Situselenization of ZIF-8/67 Polyhedron. *Appl. Surf. Sci.* **2020**, *518*, 146259. [CrossRef]

69. Chu, R.; Song, H.; Ullah, Z.; Guan, Z.; Zhang, Y.; Zhao, L.; Chen, M.; Li, W.; Li, Q.; Liu, L. ZIF-8 Derived Nitrogen-Doped Carbon Composites Boost the Rate Performance of Organic Cathodes for Sodium Ion Batteries. *Electrochim. Acta* **2020**, *362*, 137115. [CrossRef]

70. He, Y.; Wang, L.; Dong, C.; Li, C.; Ding, X.; Qian, Y.; Xu, L. In-Situ Rooting ZnSe/N-Doped Hollow Carbon Architectures as High-Rate and Long-Life Anode Materials for Half/Full Sodium-Ion and Potassium-Ion Batteries. *Energy Storage Mater.* **2019**, *23*, 35–45. [CrossRef]

71. Alam, M.W.; BaQais, A.; Nahvi, I.; Yasin, A.; Shajahan, S. Hydrothermally Synthesized Fluorine Added O_3-$NaFe_{1-x}Mg_xO_2$ Cathodes for Sodium Ion Batteries. *Inorganics* **2023**, *11*, 37. [CrossRef]

72. Fei, H.; Wu, P.; He, L.; Li, H. Facile Synthesis of Hollow V_2O_5 Microspheres for Lithium-Ion Batteries with Improved Performance. *Inorganics* **2024**, *12*, 37. [CrossRef]

73. Li, T.; Yu, G.; Song, M.; Zhang, Q.; Li, Y.; Bai, X. Facile Synthesis of Nb-Doped $CoTiO_3$ Hexagonal Microprisms as Promising Anode Materials for Lithium-Ion Batteries. *Inorganics* **2023**, *11*, 10. [CrossRef]

74. Venezia, E.; Salimi, P.; Liang, S.; Fugattini, S.; Carbone, L.; Zaccaria, R.P. Comparative Study of Lithium Halide-Based Electrolytes for Application in Lithium-Sulfur Batteries. *Inorganics* **2023**, *11*, 86. [CrossRef]

75. Zhang, J.; Xie, Z.; Ali, Z.; Li, N.; Liu, Q.; Fan, W.; Ma, J.; Sun, R. Oxygen-doped Carbon Nitride Nanocages with Efficient Photon-to-Electron Conversion for Selective Oxidation of Xylose/Xylan to Yield Xylonic Acid. *Pap. Biomater.* **2023**, *8*, 53–65. [CrossRef]

76. Ou, X.; Xiong, X.; Zheng, F.; Yang, C.; Lin, Z.; Hu, R.; Jin, C.; Chen, Y.; Liu, M. In Situ X-ray diffraction characterization of NbS_2 nanosheets as the anode material for sodium ion batteries. *J. Power Sources* **2016**, *325*, 410–416. [CrossRef]

77. Ni, Q.; Jiang, H.; Sandstrom, S.; Bai, Y.; Ren, H.; Wu, X.; Guo, Q.; Yu, D.; Wu, C.; Ji, X. A $Na_3V_2(PO_4)_2O_{1.6}F_{1.4}$ Cathode of Zn-Ion Battery Enabled by a Water-in-Bisalt Electrolyte. *Adv. Funct. Mater.* **2020**, *30*, 2003511. [CrossRef]

78. Li, W.; Hu, S.; Luo, X.; Li, Z.; Sun, X.; Li, M.; Liu, F.; Yu, Y. Confined Amorphous Red Phosphorus in MOF-Derived N-Doped Microporous Carbon as a Superior Anode for Sodium-Ion Battery. *Adv. Mater.* **2017**, *29*, 1605820. [CrossRef]

79. Zhou, L.-F.; Gao, X.-W.; Du, T.; Gong, H.; Liu, L.-Y.; Luo, W.-B. Two-dimensional NbSSe as anode material for low-temperature sodium-ion batteries. *Chem. Eng. J.* **2022**, *435*, 134838. [CrossRef]